Sustainable Energy & Fuels

Li^+ transport properties of sulfolane-based gel polymer electrolyte and effective suppression of lithium polysulfide dissolution in lithium–sulfur batteries

Journal:	*Sustainable Energy & Fuels*
Manuscript ID	SE-ART-05-2022-000711.R1
Article Type:	Paper
Date Submitted by the Author:	08-Jul-2022
Complete List of Authors:	Miyauchi, Hibiki; Kogakuin Daigaku - Hachioji Campus, Department of Environmental Chemistry and Chemical Engineering Inaba, Kohei; Kogakuin Daigaku - Hachioji Campus, Department of Environmental Chemistry and Chemical Engineering Takahashi, Keitaro; Kogakuin Daigaku - Hachioji Campus Arai, Nana; Niigata University, Graduate School of Science and Technology Umebayashi, Yasuhiro; Niigata University, Graduate School of Science and Technology Seki, Shiro; Kogakuin Daigaku - Hachioji Campus, Department of Environmental Chemistry and Chemical Engineering

Sustainable Energy & Fuels

PAPER

Li^+ transport properties of sulfolane-based gel polymer electrolyte and effective suppression of lithium polysulfide dissolution in lithium–sulfur batteries

Received 00th January 20xx,
Accepted 00th January 20xx

DOI: 10.1039/x0xx00000x

Hibiki Miyauchi,[a] Kohei Inaba,[a] Keitaro Takahashi,[a] Nana Arai,[b] Yasuhiro Umebayashi[b] and Shiro Seki*[a]

Sulfolane (SL)-based gel polymer electrolytes composed of a polyether-based host polymer were investigated for long-lifecycle lithium–sulfur batteries. The proposed electrolytes were expected to cause chemical and physical suppression of Li_2S_n dissolution and diffusion owing to the low Li_2S_n solubility, derived from the highly concentrated SL-based electrolytes, and low Li_2S_n diffusion, derived from the host polymer, respectively. The Li^+ transport properties, and Li^+–SL and Li^+–anion interactions, were analyzed by alternating current impedance measurements and Raman spectroscopy, respectively. The relationships between gel polymer electrolyte composition and Li^+ coordination structure / Li^+ transport properties were also investigated. The Li–S cells containing gel polymer electrolytes exhibited a sufficient discharge capacity in the first cycle (approx. 1,150 mAh g^{-1}) and stable charge discharge operation for 100 cycles. Application of the proposed electrolytes resulted in high battery performance owing to chemical and physical control of Li_2S_n dissolution and diffusion, and favorable electrolyte / Li metal interface formation.

1. Introduction

Lithium–sulfur batteries, comprising S_8 and Li metal as positive and negative electrodes, are expected to be candidates for next-generation energy storage systems owing to their high energy density and low cost compared with conventional lithium ion secondary batteries (LIBs). Molecular sulfur (S_8) has a theoretical capacity of 1,672 mAh g^{-1}, which is high compared with those of transition metal-based positive electrodes owing to the discharge (reduction) reaction of S_8 to Li_2S. However, several serious problems prevent the practical utilization of Li–S batteries, such as their insulation properties and the high solubility of reactive intermediates in organic liquid electrolytes.[1–4] Dissolved lithium polysulfide (Li_2S_n) increases the electrolyte viscosity and redox shuttle reactions between the negative and positive electrodes.[5–7] For example, practically applied carbonate-based solvent systems, such as ethylene carbonate (EC), diethylene carbonate (DEC), and dimethyl carbonate (DMC), readily react with Li_2S_n.[8,9] Therefore, electrolyte design to balance solubility and chemical stability is needed. Therefore, ether-based solvents, such as mixtures of 1,3-dioxolane (DOL) and dimethyl ether (DME), have been investigated in Li–S batteries since the early stages of development.[2,10,11] Recently, control of Li_2S_n dissolution has been reported using highly concentrated electrolyte solutions comprising room-temperature ionic liquids,[12–14] solvate ionic liquids,[15,16] and sulfolane (SL)-based liquid electrolytes.[17–19] Low Li_2S_n solubility in electrolyte solutions has been expressed by common physicochemical properties, namely, the relatively low donor number, dielectric constant, and Lewis acidity / basicity,[13–17,20] or the common ion effect resulting from the high concentration of carrier salts.[21,22] In particular, SL-based concentrated liquid electrolytes exhibit quite low Li_2S_n solubility with a fast ion transport mechanism owing to the specific solvate structures between solvents and anions.[17,23,24]

Poly(ethylene)oxide (PEO)-based solid polymer electrolytes are also expected to be chemically and physically stable electrolytes for Li metal negative electrodes and Li_2S_n dissolution in the electrolyte layer.[25–34] Effective control of Li_2S_2 and Li_2S formation at Li metal was expected owing to the low Li_2S_n diffusion compared with liquid electrolytes, despite the PEO-based electrolytes also obtaining slight Li_2S_n solubility derived from the repeat CH_2CH_2O– units. However, owing to their low molecular mobility and high crystallinity, 'solvent-free' PEO-based solid electrolytes lack the important properties of ionic conduction and interfacial reaction at the electrodes required for high-performance Li battery systems. To overcome these problems, genuine polymer electrolytes, filled electrolytes composed of inorganic filler,[28–31,35–37] and gel polymer electrolytes (GPEs)[32–34,38–40] have been investigated using various solvents (ether-based and carbonate-based). In general, GPEs show intermediate properties between liquid and solid states, and have already been used commercially in LIBs to prevent the formation of Li dendrite. In this case, the solvents act as plasticizing materials, providing high ionic mobility

[a] Graduate School of Applied Chemistry and Chemical Engineering, Kogakuin University, 2665-1 Nakano-machi, Hachioji, Tokyo 192-0015, Japan. Email: shiro-seki@cc.kogakuin.ac.jp; Fax: +81-42-628-4568; Tel.: +81-42-628-4568
[b] Graduate School of Science and Technology, Niigata University, 8050, Ikarashi, 2-no-cho, Nishi-ku, Niigata-shi, Niigata 950-2181, Japan.
Electronic Supplementary Information (ESI) available See DOI: 10.1039/x0xx00000x

regardless of the solubility of the functional chemical, such as Li_2S_n. In this study, we proposed solid GPEs that exhibit very low Li_2S_n solubility by compatible design according to chemical / physical considerations using an SL-based liquid electrolyte and PEO-based solid electrolyte. These electrolyte systems provide the physical advantages of suppressing both Li_2S_n diffusion and dendrite formation by metallic Li with charge / discharge processes, and the chemical advantages of Li_2S_n dissolution, and high bulk and interfacial ionic transport. The physicochemical and electrochemical properties of these GPEs, and the properties of their Li–S batteries, are reported.

2. Experimental

2.1 Preparation of gel polymer electrolytes

All processes were conducted in an argon-filled glove box ([O_2], <10 ppm; dew point, <193 K; Miwa Mfg Co., Ltd.). $LiN(SO_2CF_3)_2$ (LiTFSA) (Solvey Co., Ltd.) was dissolved in sulfolane (SL: Kishida chemical Co., Ltd.) at molar ratios (x = SL/LiTFSA) of 1, 1.5, and 2, expressed as xSL+1LiTFSA. xSL+1LiTFSA and the P(EO/PO) macromonomer (EO/PO = 8:2, M_w = *ca.* 8000, Dai-ichi Kogyo Seiyaku Co. Ltd.) were mixed at xSL+1LiTFSA weight ratios (y) of 70, 80, and 90 wt%, and 2,2-dimethoxy-2-phenylacetophenone (DMPA, Chiba Japan K.K) was added as the photoinitiator (0.1 wt% based on P(EO/PO)). Photopolymerization was conducted by UV irradiation for 5 min to obtain self-standing transparent gel polymer electrolytes (GPEs).

2.2 Thermal analysis

The thermal properties of the GPEs were investigated using thermogravimetry‐differential thermal analysis (TG-DTA, Thermo Plus EVO2 analyzer, Rigaku) and differential scanning calorimetry (DSC, Thermo Plus EVO2 analyzer, Rigaku). TG-DTA measurements conducted from 303.15 to 743.15 K at heating scan rate of 10 K min^{-1}. DSC measurements were conducted with cooling from 303.15 K to 173.15 K and heating to 373.15K using a cooling / heating scan rate of 10 K min^{-1}.

2.3 Raman spectroscopy

Raman spectra were measured to investigate the interaction and ionic state of the prepared GPEs. A glass tube (ϕ = 5 mm, l = 60 mm) was filled with the electrolyte solution (SL/LiTFSA/P(EO/PO)/DMPA mixture), followed by photopolymerization under UV irradiation for 14 min. All Raman measurements were conducted using RMP-510 (Jasco) at room temperature. Raman spectra were measured at 400 mW and 514.6 nm with an optical resolution of 2.7 cm^{-1}, and the obtained Raman spectra were fitted with the pseudo-Voight function.

2.4 Electrochemical measurements

The ionic conductivity (σ) of GPEs was measured by alternating current (AC) impedance measurements (VSP, Bio Logic). The GPE films were cut into circles with a diameter of 12 mm and sandwiched between SUS electrodes as blocking electrodes. AC impedance measurements were conducted by cooling from 353 K to 220 K with a frequency range of 200 kHz to 50 mHz and an amplitude of 100 mV from 353 K to 263 K or 500 mV from 263 K to 220 K. The samples were thermally equilibrated at each temperature for at least 90 min prior to measurement.

The interfacial properties between GPEs and the Li metal electrode were measured by [Li|GPE|Li] symmetric cells using a 2032-type coin cell. The cells were stored at 333 K for 1400 h and AC impedance measurements were conducted every 5 h in the frequency range of 200 kHz to 10 mHz with an amplitude of 10 mV. The temperature dependence of the cells was measured in the range of 353 to 283 K using both heating and cooling processes. To evaluate the Li^+ transport number, low-frequency AC impedance measurements were conducted using [Li|GPE|Li] symmetric cells in the frequency range of 200 kHz to 10 μHz with an amplitude of 10 mV at 333 K.

2.5 Charge–discharge measurements of lithium–sulfur battery

A Li–S battery was prepared using a S_8 positive electrode, GPE (x=1.5, y=80wt%), liquid electrolyte (1.5SL+1LiTFSA), and Li metal negative electrode. The S_8 positive electrode sheet was prepared using S_8 (Japan Pure Chemical Co., Ltd.) as the positive electrode active material, Ketjenblack (KB, ECP-600JD, Lion Co.), and polyvinyl pyrrolidone (PVPK90, Fujifilm Wako Pure Chemical Co.) as components. An S_8/C mixture was obtained by holding KB and S_8 mixed with weight ratio of 2:1 at 438 K for 10 h under vacuum. The S_8/C mixture and PVPK90 (S_8/KB/PVP weight ratio of 56.7:28.3:15) were dispersed in EtOH and applied to Al foil (electrode loading, 0.53 mg-S_8 cm^{-2}). After drying under vacuum at 333 K for 10 h, the sheet was cut into circle with a diameter of 16 mm. The obtained S_8 positive electrode was pressed at 1.5 t for 30 s using a uniaxial press. The GPE film and Li foil were cut into circles with diameters of 19 mm and 16 mm, respectively. [Li|GPE|S_8] cells were fabricated using a 2032-type coin cell. For cell fabrication, the liquid sample (x = 1.5) was dropped onto the S_8 positive electrode to maintain sufficient penetration and a continuous ionic conductive pathway. The amount of liquid sample was also regulated at y < 90 wt% to avoid phase separation of the host polymer and liquid electrolyte (*vide infra*). The assembled [Li|GPE|S_8] cells were stored at 333 K for 24 h for heat annealing, and constant-current charge–discharge measurements were conducted at 3.3–1.0 V, C/18 , and 303 K. Also, the C-rate is a measure of the rate (current) at which a prepared cell is completely charged or discharged, relative to theoretical capacity of based active material S_8 (1672 mAh g^{-1}).

3. Results and Discussion

3.1 Thermal Properties

Figure 1 shows the TG curves of the prepared GPEs, with the sample data for x = 1–2 and y = 90 wt% shown in Figure S1. Compared with neat SL, different weight-reduction tendencies were observed between 400 and 600 K in the TG curves of the prepared GPEs. In this study, WP_{SL} is defined as the weight percentage of SL in GPE. The black solid circle plots represent the evaporation (or decomposition) temperature of SL, if weight changes in GPE occurred with increasing temperature following SL, P(EO/PO

), and LiTFSA, respectively. For all x values, the thermal stability of the GPEs improved with increasing y values (ratio of liquid electrolyte). Dennis *et al*. reported the sufficient thermal stability of highly concentrated Li^+ liquid electrolytes owing to the strong interaction between Li^+ and solvent molecules.[41] For the GPEs, Li cations should interact with both the solvent (=O) and host polymer

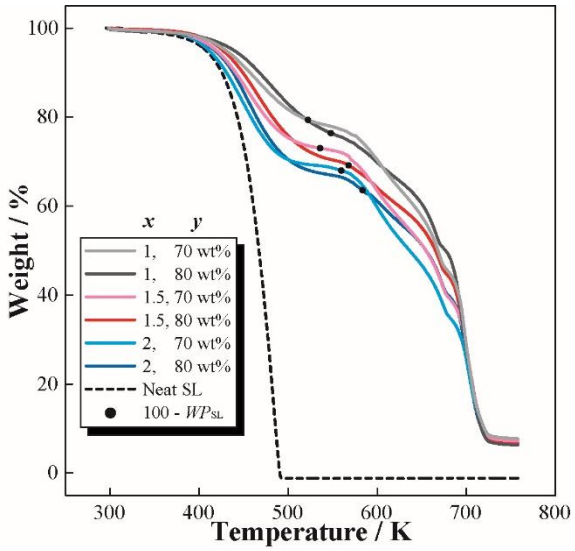

Fig. 1 TG curves of GPEs in different ratios of SL, LiTFSA, and P(EO/PO) (x = 1–2, y = 70 and 80 wt%).

(–O–). Therefore, the coordination balance of the SL–LiTFSA electrolyte changed with the introduction of P(EO/PO) containing ether oxygen moieties. Figure 2(a) shows the DSC thermograms of the prepared GPEs, with the sample data for x = 1–2 and y = 90 wt% shown in Figure S2. Thermal capacity changes attributed to the glass transition were observed in the DSC thermograms of all GPEs, with the obtained data indicating compatibility between the liquid electrolyte and host polymer,[42] in particular, ether oxygen of P(EO/PO) and Li cations. Although at $y \leq 80$ wt%, single glass transition thermal behavior derived from the homogeneous phase was observed, samples with y = 90 wt% exhibited two separate glass transitions owing to phase separation of the saturated liquid electrolyte. Figure 2(b) shows the glass transition temperatures (T_g) calculated from DSC thermograms, except for samples with y = 90 wt%. The T_g values decreased with a decreasing x value (molar ratio of SL/LiTFSA), and drastically decreased at y = 80 wt% owing to the decreased cross-linking density of the GPE electrolyte resulting from the difference in complexation ability between the O atoms of polyether and sulfolane. Therefore, the prepared GPEs should consist of a plasticizer (SL/LiTFSA) and host polymer (P(EO/PO)) with sufficient balance of strong and weak interaction energies, each other.

3.2 Ionic Conductive Properties of Prepared GPEs

Figure 3 shows the temperature dependence of the ionic conductivity (σ) of the prepared GPEs using Arrhenius-type plots, with sample data for x = 1–2 and y = 90 wt% shown in Figure S3. Vogel–Fulcher–Tammann (VFT)-type temperature behavior[43–45] was observed in the σ values of all GPEs. Generally, σ in a unit volume is defined as follows:

$$\sigma = \sum_j n_j q_j \mu_j \quad (1)$$

where n, q, and μ are the number, charge, and mobility of the carrier ions in the specific volume, respectively. The suffix j corresponds to the Li cation and TFSA anions. In this case, q is always expressed as 1, and the σ values should depend on both n (related to the carrier density and ionic dissociation degree) and μ (related to the

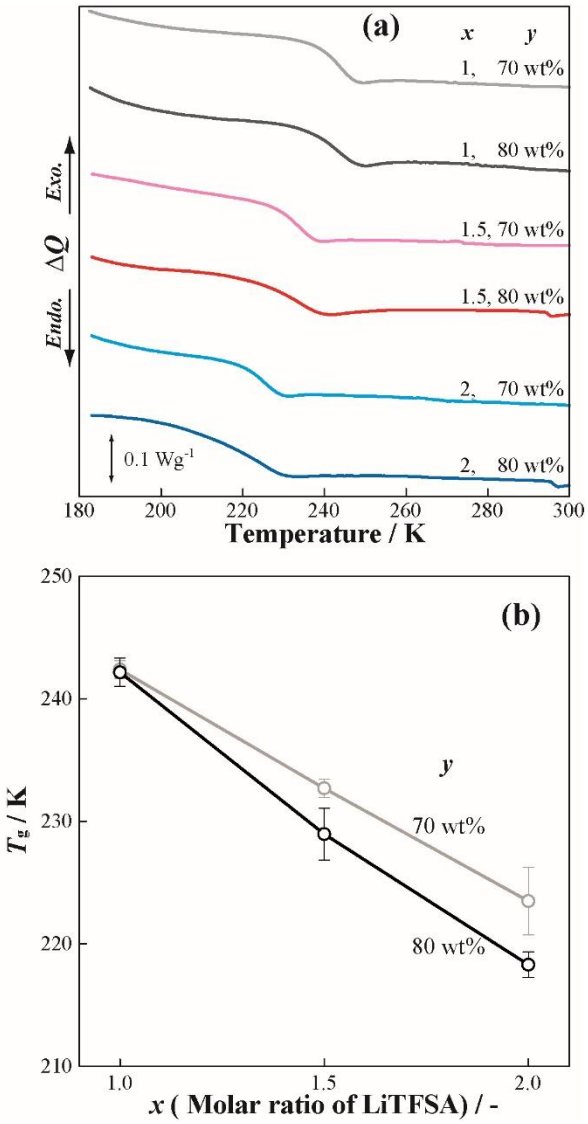

Fig. 2 (a) DSC thermograms and (b) glass transition temperatures of GPEs in different ratios of SL, LiTFSA, and P(EO/PO) (x = 1–2, y = 70 and 80 wt%).

macroscopic viscosity and ionic diffusion constants). The highest σ value of 0.46 mS cm^{-1} at 303.15 K was observed for the sample with x = 2 and y = 80 wt%, despite the liquid sample with x = 2 exhibiting a σ value of 0.42 mS cm^{-1} at the same temperature. In particular, n should be dependent on the x^{-1} and y values from the carrier density of the GPE electrolytes, respectively. However, the DSC data (T_g values) showed that the ionic mobility also improved with both x and y values. If GPE electrolytes contained a sufficient amount of carrier Li^+, such as x = 1, the T_g values of the GPE electrolytes did not change, despite the clear change in y values obtained. However, at low carrier concentration, such as x = 2, the σ values increased with y owing to changes in the thermal properties (ionic mobility). Therefore, the main contributor to the σ value might be y, which strongly corresponded with the thermal properties of the GPE electrolytes.

3.3 Raman Spectroscopy

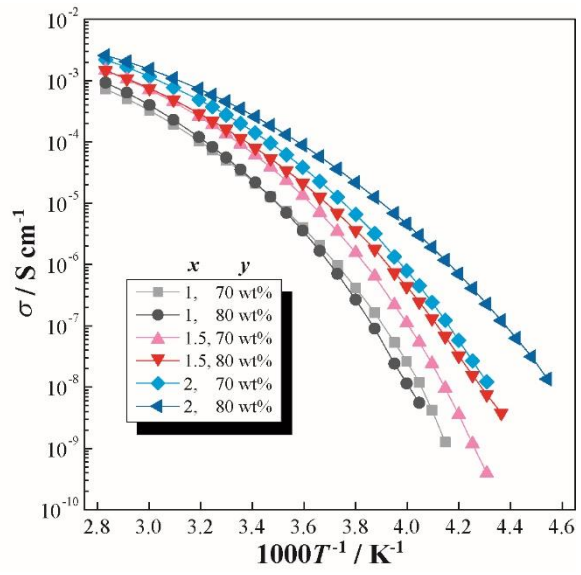

Fig. 3 Arrhenius-type temperature dependence of ionic conductivity of GPEs in different ratios of SL, LiTFSA, and P(EO/PO) (x = 1–2, y = 70 and 80 wt%).

To investigate the coordination structure among the ionic species (Li^+ and $TFSA^-$), matrix (P(EO/PO)), and solvent (SL), Raman spectra were recorded to assign several vibrational modes. To provide a full overview of the Raman spectra of the prepared GPEs (x = 2, y = 70, 80, and 90 wt%) and the liquid electrolyte with x = 2 and y = 100 wt%, Figure S4 shows the spectra over the wide wavenumber range of 200–1400 cm^{-1}. Analyzable changes and shifts in peak position, which should be affected by interactions with Li^+ according to the vibrational modes of C–O–C bonds in P(EO/PO),[46] were not confirmed with composition changes and absence / presence of the P(EO/PO) host polymer. This study mainly focused on the coordination structure SL and $TFSA^-$ that should affect the both the δSO_2 and the νSN coupled with the δCF_3 modes, respectively. Figure 4 shows the Raman spectra of GPEs and the liquid electrolyte in the frequency ranges of 540–610 cm^{-1} and 700–800 cm^{-1}. Broad peaks observed at approx. 565–590 cm^{-1} were attributed to the δSO_2 mode of SL. According to previous reports, the peak for the δSO_2 mode of neat (free) SL was observed at 568 cm^{-1},[47] with Dokko *et al*. reporting that this shifted toward the higher wavenumber corresponding to the monodentate and the bidentate SL structures with Li^+ owing to the formation of coordination transitions.[17,23] In the observed Raman spectra, the peaks shifted to the higher wavenumber with increasing y values. Therefore, introducing P(EO/PO) should decrease the amount of bidentate or monodentate SL molecules and generate free (non-coordinated) SL molecules. Other weak vibrational modes, such as the δSO_2 and δCF_3 modes of $TFSA^-$, were also observed in this region.[48] Therefore, precise analysis by peak deconvolution of the Raman spectra using non-linear least-squares curve fitting analysis was quite difficult. Strong and broad peaks were observed at 730–750 cm^{-1}, which were attributed to the νSN mode coupled with the δCF_3 mode of $TFSA^-$ (expressed as [νSN + δCF_3]).[48–51] [νSN + δCF_3] was sensitively affected by the coordination structure of $TFSA^-$. Therefore, the peak shift occurred in the order of noncoordinated or solvent-separated ion pair (expressed free), contact ion pair (CIP), and aggregates (AGGs), owing to the formation of a successive coordination structure from both SL and $TFSA^-$.[49–51] To investigate the relationship between the GPE composition and $TFSA^-$ coordination structure, the Raman spectra were precisely analyzed by non–linear least-squares curve fitting analysis using pseudo-Voigt function (Figures S4(b) and

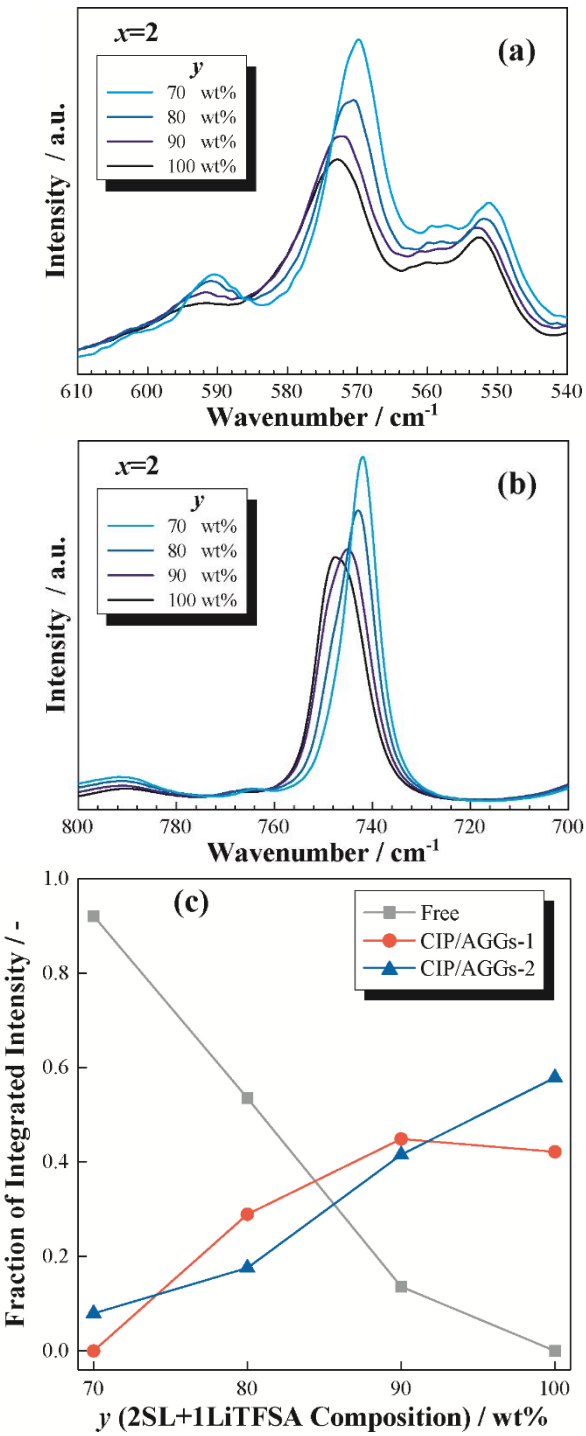

Fig. 4 Raman spectra of GPEs (x = 2, y = 70–90 wt%) and 2SL+1LiTFSA (x = 2, y = 100 wt%) in ranges of (a) 540–610 cm^{-1} and (b) 700–800 cm^{-1}, and (c) fractions of peak integration for free, CIP/AGGs-1, and CIP/AGGs-2 anions attributed to $\nu SN+\delta CF_3$ mode.

S4(c)).[52] Assignments of vibration modes and calculated peaks are listed in Table S1. The calculated peaks at 742, 745, and 749 cm^{-1} were assigned to free, two-type clusters (CIP/AGGs-1, and CIP/AGGs-2 of $TFSA^-$), respectively. Figure 4(c) shows the fractions of peak integration for free, CIP/AGGs-1, and CIP/AGGs-2 calculated from the Raman spectra between 600 and 775 cm^{-1}. The fraction of peak integration for free $TFSA^-$ linearly increased with an increasing P(EO/PO) amount, and $TFSA^-$ preferentially existed as a free anion at y = 70 wt%. In contrast, the fraction of peak integration for CIP/AGGs-1 and 2 decreased with the holding constant ratio between CIP/AGGs-1 and CIP/AGGs-2, and some $TFSA^-$ might form successive coordination structures in GPEs. Therefore, the introduction of P(EO/PO) (solidification of electrolytes) might lead to a decreasing tendency in the successive coordination structure of SL-LiTFSA (highly conductive Li hopping route),[23] and changes in the coordination structure (conductive pathway) were expected with an excessive amount of P(EO/PO).

3.4 AC Impedance Measurements of Li/Li Symmetric Cells

Figure 5(a) shows the storage time dependence of Nyquist plots of the [Li|GPE|Li] symmetric cell with x = 1.5 and y = 80 wt% at 333.15 K, with the bulk resistance component subtracted for simplification (Nyquist plot containing bulk resistance components is shown in Figure S5). The equivalent circuit was used to analyze the Nyquist plots obtained at 333.15 K, as shown in Eq. 2:

$$R_b + R_{Li} / Q_{Li} + R_{Cell} / Q_{Cell} + Z_w \quad (2)$$

where R_b is the bulk resistance, R_{Li} is the GPE/Li metal interfacial resistance, and Z_w is the Warburg impedance component. R_{Cell} was assumed according to the resistance component passivation film expected for the SEI film or other factors.[53,54] Q_{Li} and Q_{Cell} are the constant phase elements of the corresponding aforementioned components.

Semicircular arcs in the high-frequency region (100 kHz to 200 Hz) and deformative arcs in the middle-frequency region (200 Hz to 400 mHz) were attributed to R_{Li} and R_{Cell}, respectively, and R_{Li} should contain charge transfer and Li^+ transfer processes at the SEI film. Although R_b exhibited relatively unstable values with storage time (Figure S5), the cell after storage tests showed stable R_b values of approx. 20 Ω cm^2 from other analyses (*vide infra*) without significant degradation. In contrast, the R_{Li} values increased with storage time, suggesting SEI film growth on the Li metal surface. However, the R_{Cell} values were almost constant with storage time, indicating that this was the resistance component of the passivation film, except for the SEI film or other factors, such as metallic conduction and cell resistances.[53,54] Next, the R_{Li} values were investigated to analyze the SEI formation / growth processes. Figure 5(b) shows the storage time dependence of R_{Li} calculated from the impedance spectra of [Li|GPE|Li] symmetric cells (dashed line represents interruption of measurement). Low R_{Li} values of less than 50 Ω cm^2 were observed at 333.15 K after 1400 h with a certain increase in all cells, but the specific dependence on the GPE composition of R_{Li} was not confirmed. In general, SEI films have been reported to form between Li metal and PEO-based electrolytes with a high resistance of approx. 100 Ω cm^2,[55–57] while PEO-based electrolytes provide sufficient reductive stability. In contrast, SL exhibits a low reductive stability for Li metal, and generation of a passivation film on the Li metal

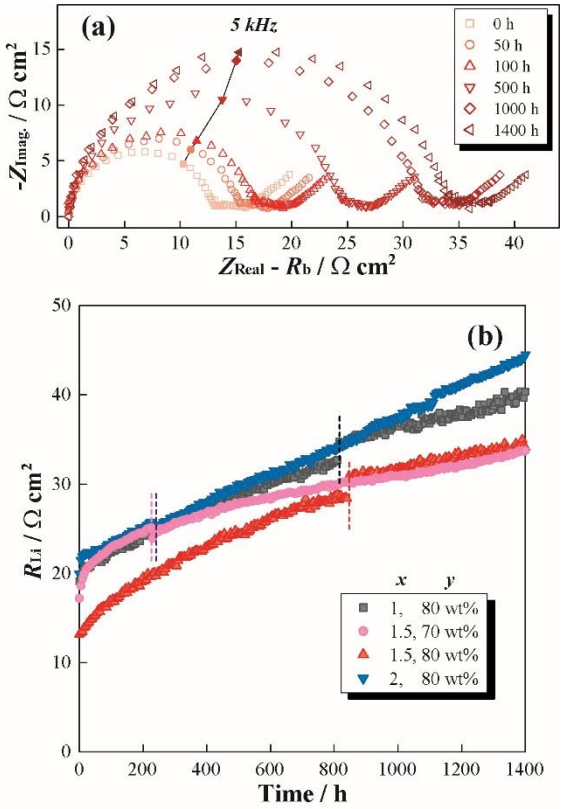

Fig. 5 Storage time dependence of (a) Nyquist plots of [Li|GPE(x = 1.5, y = 80 wt%)|Li] symmetric cell (for simplicity, R_b values were subtracted), and (b) GPE/Li metal interfacial resistance (R_{Li}) at 333 K.

surface was reported owing to continuous reductive decomposition of SL, even for highly LiTFSA concentrated electrolytes, such as x = 2.[58] According to the reductive stability of SL,[58–61] a continuous increase in the R_{Li} values should indicate preferential reductive decomposition of SL in the GPE. In fact, decreased reductive stability of SL was suggested by the Raman spectra of GPEs and in the case of liquid electrolytes owing to the existence of free SL molecules. However, the obtained R_{Li} values were quite low owing to the relatively high stability of solid electrolytes. The data suggested that sufficient passivation film formation with both low resistance, attributed to the highly concentrated SL-LiTFSA 'active' interface, and chemical stability, attributed to the PEO-based 'stable' interface, was obtained by fabricating GPEs.

The temperature dependence of R_{Li} was investigated using [Li|GPE|Li] symmetric cells for characterization of the charge transfer process at the electrolyte / Li metal interface. Figure 6(a) shows the Nyquist plots of [Li|GPE|Li] symmetric cells with x = 1.5 and y = 80 wt% at 333, 343, and 353 K. Notable changes in the Nyquist plots were not observed between cooling and heating processes, and the temperature dependence of R_{Li} should be discussed without consideration of SEI film growth derived from GPE decomposition with storage time. Figure 6(b) shows the temperature dependence of the R_{Li} values using Arrhenius-type plots. R_{Li} was calculated using the equivalent circuit, as shown in Eq. 2, to obtain impedance spectra between 313 and 353 K. In contrast,

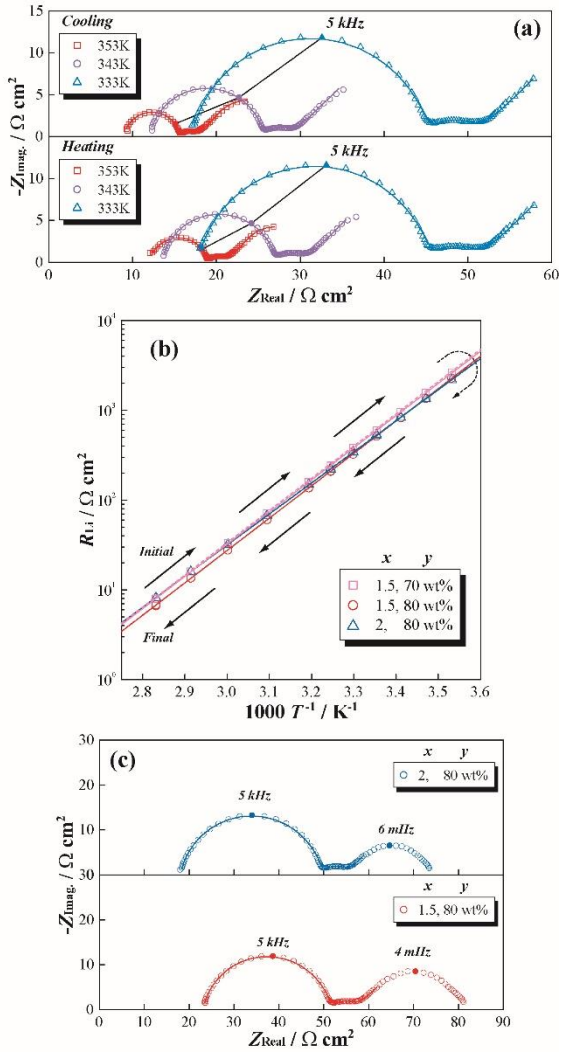

Fig. 6 Temperature dependence of (a) Nyquist plots of [Li|GPE|Li] symmetric cells at 333, 343, and 353 K, (b) GPE/Li metal interfacial resistance (R_{Li}), and (c) Nyquist plots of [Li|GPE|Li] symmetric cells in the low frequency region at 353 K.

impedance spectra of the R_{Cell} / Q_{Cell} component could not be sufficiently observed under the setup frequency conditions. Therefore, the R_{Li} values were calculated using the following equivalent circuit between 283 and 308 K:

$$R_b + R_{Li} / Q_{Li} \quad (3)$$

The obtained R_{Li} values showed Arrhenius-type temperature dependence, and were calculated using the Arrhenius equation shown in Eq. 4:

$$k \propto 1/R_{Li}, k = A \exp(-E_a/RT) \quad (4)$$

where k, A, and R are the reaction rate constant, frequency factor, and gas constant, respectively, and E_a is the apparent activation energy, which should be related to the activation barrier of the Li^+ solvation / desolvation process in the charge transfer reaction.[62–64] Regression lines for the cooling process (solid line) and heating process (dashed line) are also indicated in Figure 6(b), with both

Table 1. Apparent activation energies calculated from GPE/Li metal interfacial resistance and Li^+ transport numbers from low-frequency impedance spectra

	E_a / kJ mol^{-1}	
	Cooling	**Heating**
***x* = 1.5, *y* = 70 wt%**	68.6	68.7
***x* = 1.5, *y* = 80 wt%**	69.1	69.0
***x* = 2, *y* = 80 wt%**	66.3	66.3

calculated E_a values (Table 1) being almost the same, at less than 70 kJ mol^{-1}, in all cells compared with conventional solvent-free PEO-based electrolytes.[56,65] In previous studies, relatively high E_a values of about 70–100 kJ mol^{-1} were reported for PEO-based electrolyte / Li metal interfacial resistance.[56,65] In contrast, increasing trends for E_a have been reported with Li salt concentration (including concentrated liquid electrolytes) owing to the strong ion–ion interaction energies derived from the CIP and AGGs structures,[62,63] while intermediate E_a values of 50–70 kJ mol^{-1} have been reported between conventional liquid electrolytes (i.e., 1.0 mol kg^{-1}) and solvent-free solid electrolytes.[62–64] The existence of CIP and AGGs of GPE was also confirmed by Raman spectra, as shown in Figure 4. Therefore, similar solvation / desolvation processes should occur with highly concentrated SL–LiTFSA liquid electrolytes. In other words, the charge transfer reaction involved in the solvation / desolvation processes of SL–LiTFSA complexes should actively occur at the GPE/Li metal interface. Figure 6(c) shows Nyquist plots of [Li|GPE|Li] symmetric cells using samples with x = 1.5 and y = 80 wt%, and x = 2 and y = 80 wt%, in the frequency range of 200 kHz to 10 μHz at 333 K. Another semicircular arc, in addition to R_{Li}, was confirmed in the low frequency region (400 mHz to 10 μHz), and the following equivalent circuit was assumed:

$$R_b + R_{Li} / Q_{Li} + R_{Cell} / Q_{Cell} + Z_d \quad (5)$$

where Z_d is the finite-length diffusion resistance. The obtained Z_d components exhibited semicircular shapes without the gentle slopes of more than 45 degree attributed to Z_d.[65] The terminatory point was used to calculate Z_d. Furthermore, the Li^+ transport number (t_{Li+}) was calculated using the following equation:[65,66]

$$t_{Li+} = R_b / (R_b + Z_d) \quad (6)$$

The resistance values calculated from the assumed equivalent circuit and t_{Li+} values are listed in Table S2. Both electrolytes exhibited relatively high t_{Li+} values of 0.49 [-] as PEO-based solid electrolytes.[56,67] In previous reports, t_{Li+} values of over 0.6 [-] were confirmed in SL-based highly concentrated liquid electrolytes using the PGSE-NMR method and potentiostatic polarization combined with electrochemical impedance spectroscopy, and should be caused by continuous coordination structure of SL and $TFSA^-$.[17,24] In fact, reversible plating / stripping properties of Li was also confirmed using [Li/Ni] cell by cyclic volltammetry (Figure S6). Therefore, high Li^+ transport by the GPEs should occur with the specific coordination

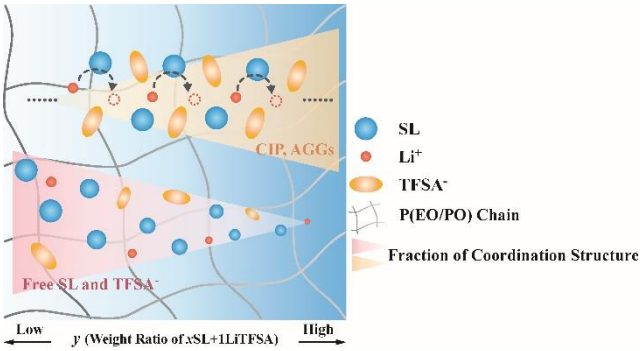

Fig. 7 Schematic image of relationship between GPE composition and Li^+ coordination structure/Li^+ transport properties.

structure of SL and $TFSA^-$ in the high Li salt concentration region. The slight decrease in the t_{Li+} value compared with SL–LiTFSA liquid electrolytes might be due to the Li^+ transport behavior derived from the coordination ability and relatively slow segmental motion of the P(EO/PO) chain. Furthermore, interruption of the extended the specific coordination structure SL–LiTFSA complexes has been reported in presence of HFE.[17] Therefore, a similar effect might occur by introducing P(EO/PO). Figure 7 shows a schematic image of the relationship of between GPE composition and Li^+ coordination structure / Li^+ transport properties in the prepared GPEs. In liquid electrolytes with a high Li salt concentration (right side), few free solvent and anion molecules were present, and a continuous coordination structure including CIP and AGGs formed to contribute high Li^+ transport. In contrast, in the proposed GPEs (left side), ether oxygen introduced by the P(EO/PO) chain behaved as a ligand of Li^+, interacting competitively with SL and $TFSA^-$. This competitive interaction should affect the fraction of continuous coordination structures, such as CIP and AGGs. In this study, interaction energies between Li^+ and P(EO/PO) were weaker than that of SL. Therefore, the high Li^+ transport properties derived from the continuous coordination structure of the SL–LiTFSA complex were confirmed, even in the case of GPEs.

3.5 Charge–Discharge Properties of Li–S Battery

Figure 8 shows the charge–discharge profiles, cycle number-dependence of charge and discharge capacity, and the calculated Coulombic efficiency of the prepared [Li|GPE|S_8] coin cell for 100 cycles. The discharge curves exhibited two voltage plateaus derived from the reduction process of S_8 to Li_2S_n. Stable charge–discharge operation was achieved over 100 cycles with high Coulombic efficiency (99.7 % at 100 cycles), despite the initial irreversible capacity being relatively high (first discharge capacity, 1146 mAh g^{-1}). Furthermore, notable changes in the overvoltage were not observed, suggesting the formation of stable GPE / electrode (Li metal and Li_2S_n) interfaces and the suppression of dendrite formation by solidification. In particular, significant capacity retention was confirmed compared with conventional Li–S battery systems.[15,16] This suggested sufficient suppression of Li_2S_n dissolution at the positive electrode / GPE interfaces (without color changes of GPE film with charge/discharge process), even though some free SL molecules were present in the GPE, in which Li_2S_n was relatively soluble. Furthermore, a favorable

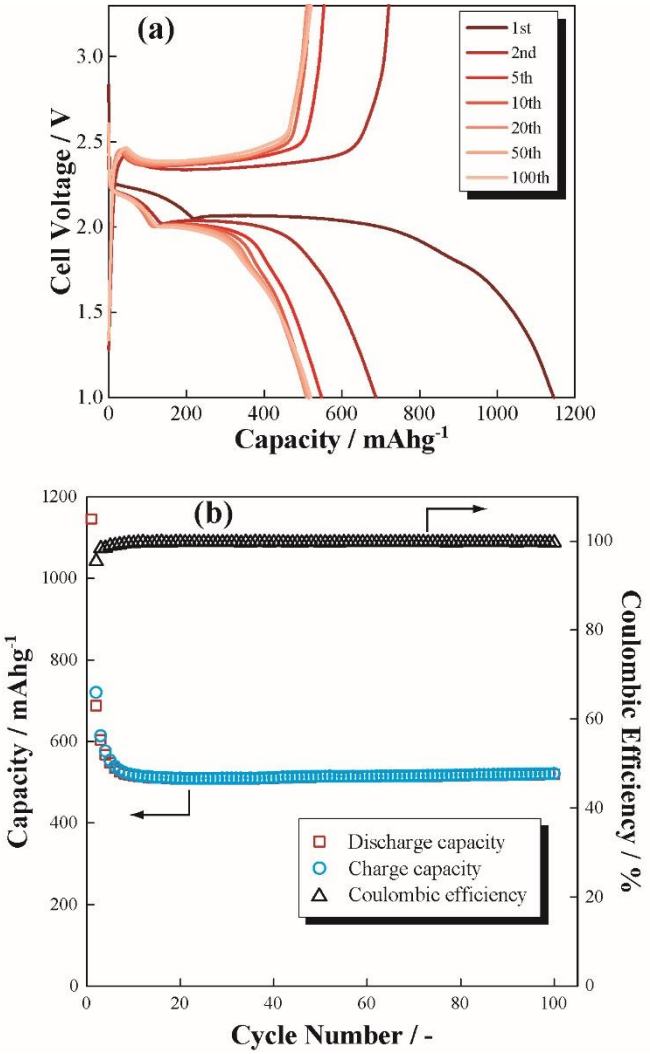

Fig. 8 (a) Charge–discharge profiles and (b) cycle number dependence of charge and discharge capacity and calculated Coulombic efficiency for the [Li|GPE|S_8] cell at 303 K.

GPE / Li metal electrode interface might be formed by physical suppression of the diffusion of high-order Li_2S_n (n = 4–8) and its reduction to Li_2S_2 or Li_2S. Therefore, the proposed GPE contributed to high battery performance for degradation control of both the S_8 positive and Li metal negative electrodes by chemical and physical effects.

4. Conclusions

GPEs consisting of an SL-based highly concentrated electrolyte and P(EO/PO) host polymer were prepared, and their physicochemical and electrochemical properties were investigated. The SL–LiTFSA liquid electrolyte functioned as a plasticizer in GPEs, and comparable ionic conduction properties to the SL–LiTFSA liquid electrolyte were observed for the sample with x = 2 and y = 80 wt% (0.46 mS cm^{-1} at 303.15 K) owing to sufficient ion mobility. Competitive interactions of each SL, $TFSA^-$, and P(EO/PO) with Li^+ were suggested by Raman spectra according to the generation monodentate or free SL and free $TFSA^-$. Furthermore, a high Li^+ transport number of 0.49 [-] was

achieved by the GPEs, and the specific coordination structure (hopping transport) of the SL–LiTFSA complex should be maintained in the GPEs. Furthermore, quite low electrolyte / Li metal interfacial resistance (<50 Ω cm^2 at 333.15 K) and a relatively low apparent activation energy (<70 kJ mol^{-1}) were observed by AC impedance measurements of [Li|GPE|Li] symmetric cells, despite the low electrochemical stability of SL molecules observed with weaker interactions between SL and Li^+ compared with highly concentrated SL–LiTFSA electrolytes. Favorable passivation film formation at the GPE/Li metal interface was suggested by impedance measurements ([Li/Li] cell) and cyclic volttametry ([Li/Ni] cell), respectively, and the prepared Li–S cell achieved stable charge discharge operation for 100 cycles. Therefore, the proposed GPEs contributed to the dissolution and diffusion of Li_2S_n at the GPE / S_8 positive electrode interface, and reductive decomposition of SL at the GPE / Li metal negative electrode interface, and achieved improved Li–S battery performance.

Conflicts of interest

There are no conflicts of interest to declare.

Acknowledgements

This work was partially supported by the Advanced Low Carbon Technology Research and Development Program (ALCA), SPRING Grant JPMJAL1301 from Japan Science and Technology Agency (JST), Japan.

References

1 R. D. Rauh, K. M. Abraham, G. F. Pearson, J. K. Surprenant and S. B. Brummer, *J. Electrochem. Soc.*, 1979, **126**, 523−527.
2 A. Manthiram, Y. Fu, S. H. Chung, C. Zu and Y. S. Su, *Chem. Rev.*, 2014, **114**, 11761−11787.
3 M. Yanagi, K. Ueno, A. Ando, S. Li, Y. Matsumae, J. Liu, K. Dokko and M. Watanabe, *J. Electrochem. Soc.*, 2020, **167**, 170531.
4 Y. Liu, Y. Elias, J. Meng, D. Aurbach, R. Zou, D. Xia and Q. Pang, *Joule*, 2021, **5**, 2323−2364.
5 Y. Diao, K. Xie, S. Xiong and X. Hong, *J. Power Sources*, 2013, **235**, 181-186.
6 F. Fan, M. Pan, K. Lau, R. Assary, W. Woodford, L. Curtiss, W. Cater and Y. Chiang, *J. Electrochem. Soc.*, 2016, **163**, A3111−A3116.
7 Y. Mikhaylik and J. Akridge, *J. Electrochem. Soc.*, 2004, **151**, A1969.
8 J. Gao, M. A. Lowe, Y. Kiya and H. D. Abruna, *J. Phys. Chem. C*, 2011, **115**, 25132−25137.
9 T. Yim, M. Park, J.Yu, K. J. Kim, K. Y. Im, J. Kim, G. Jeong, Y. N. Jo, S. Woo, K. S. Kang, I. Lee and Y. Kim, *Electrochim. Acta*, 2013, **107**, 454−460.
10 W. Wang, Y. Wang, Y. Huang, C. Huang, Z. Yu, H. Zhang, A. Wang and K. Yuan, *J. Appl. Electrochem.*, 2010, **40**, 321−325.
11 K. Seok, J. Yongju and S. L. Hong, *Electrochim. Acta*, 2004, **50**, 889−892.
12 J. H. Shin and E. J. Cairns, *J. Power Sources*, 2008, **177**, 537-545.
13 J. Park, K. Yamauchi, E. Takashima, N. Tachikawa, K. Ueno, K. Dokko and M. Watanabe, *J. Phys. Chem. C*, 2013, **117**, 4431−4440.
14 J. Park, K. Ueno, N. Tachikawa, K. Dokko and M. Watanabe, *J. Phys. Chem. C*, 2013, **117**, 20531−20541.
15 S. Seki, N. Serizawa, K. Takei, Y. Umebayashi, S. Tsuzuki and M. Watanabe, *Electrochemistry*, 2017, **85**, 680–682.
16 K. Dokko, N. Tachikawa, K. Yamauchi, M. Tsuchiya, A. Yamazaki, E. Takashima, J. Park, K. Ueno, S. Seki, N. Serizawa and M. Watanabe, *J. Electrochem. Soc.*, 2013, **160**, A1304−A1310.
17 A. Nakanishi, K. Ueno, D. Watanabe, Y. Ugata, Y. Matsumae, J. Liu, L. M. Thomas, K. Dokko and M. Watanabe, *J. Phys. Chem. C*, 2019, **123**, 14229−14238.
18 E. V. Karaseva, E. V. Kuzmina, D. V. Kolosnitsyn, N. V. Shakirova, L. V. Sheina and V. S. Kolosnitsyn, *Electrochim. Acta*, 2019, **296**, 1102−1114.
19 J. Liu, M. Marium, B. Wang, K. Ueno and M. Watanabe, *Sustain. Energy Fuels*, 2021, **5**, 1821−1831.
20 Y. Yamada and A. Yamada, *J. Electrochem. Soc.*, 2015, **162**, A2406−A2423.
21 K. Sun, N. Li, D. Su and H. Gan, *J. Electrochem. Soc.*, 2019, **166**, A50−A58.
22 E. Shin, K. Kim, S. Oh and W. Cho, *Chem. Commun.*, 2013, **49**, 2004−2006.
23 K. Dokko, D. Watanabe, Y. Ugata, L. M. Thomas, S. Tsuzuki, W. Shinoda, K. Hashimoto, K. Ueno, Y. Umebayashi and M. Watanabe, *J. Phys. Chem. B*, 2018, **122**, 10736−10745.
24 K. Shigenobu, K. Dokko, M. Watanabe and K. Ueno, *Phys. Chem. Chem. Phys.*, 2020, **22**, 15214−15221.
25 X. Judez, H. Zhang, C. Li, J. A. González-Marcos, Z. Zhou, M. Armand and L. M. Rodriguez-Martinez, *J. Phys. Chem. Lett.*, 2017, **8**, 1956−1960.
26 J. Qian, B. Jin, Y. Li, X. Zhan, Y. Hou and Q. Zhang, *J. Energy Chem.*, 2021, **56**, 420−437.
27 D. Marmorstein, T. H. Yu, K. A. Striebel, F. R. Mclarnon, J. Hou and E. J. Cairns, *J. Power Sources*, 2000, **89**, 219−226.
28 X. Tao, Y. Liu, W. Liu, G. Zhou, J. Zhao, D. Lin, C. Zu, O. Sheng, W. Zhang, H. W. Lee and Y. Cui, *Nano Lett.*, 2017, **17**, 2967−2972.
29 Y. Song, Y. Shi, J. Wan, S. Lang, X. Hu, H. Yan, B. Liu, Y. Guo, R. Wen and L. Wan, *Energy Environ. Sci.*, 2019, **12**, 2496−2506.
30 H. H. Shin, K. W. Kim, H. J. Ahn and J. H. Ahn, *Mater. Sci. Eng. B*, 2002, **95**, 148−156.
31 X. Li, H. Wang, H. Yan, Z. Gong and Y. Yang, *ACS Appl. Mater. Interfaces*, 2019, **11**, 22745−22753.
32 Q. Wang, Z. Wen, J. Jin, J. Guo, X. Huang, J. Yang and C. Chen, *Chem. Commun.*, 2016, **52**, 1637−1640.
33 J. Chen, W. A. Henderson, H. Pan, B. R. Perdue, R. Cao, J. Z. Hu, C. Wan, K. S. Han, K. T. Mueller, J. G. Zhang and Y. Shao, *Nano Lett.*, 2017, **17**, 3061−3067.
34 H. Pei, R. Guo, Y. Li, C. Fang, Y. Zhang, W. Liu, Y. Wang and J. Zie, *J. Electrochem. Soc.*, 2019, **166**, A5215−A5220.
35 Y. Liu, J. Lee and L. Hong, *J. Power Sources*, 2004, **129**, 303−311.
36 H. Croce, R. Curini, A. Martinelli, L. Persi, F. Ronci, B. Scrosati and R. Caminiti, *J. Phys. Chem. B*, 1999, **103**, 10632−10638.
37 F. Croce, L. Persi, B. Scrosati, F. Serraino-Fiory, E. Plichta and M. Hendrickson, *Electrochim. Acta*, 2001, **46**, 2457−2461.
38 W. Li, Y. Pang, J. Liu, G. Liu, Y. Wang and Y. Xia, *RSC Adv.*, 2017, **7**, 23494−23501.
39 J. Song, Y. Wang and C. Wan, *J. Power Sources*, 1999, **77**, 183−197.
40 K. Zaghib, P. Charest, A. Guerfi, J. Shim, M. Perrier and K. Striebel, *J. Power Sources*, 2004, **134**, 124−129.
41 D. W. McOwen, D. M. Seo, O. Borodin, J. Vatamanu, P. D. Boyle and W. A. Henderson, *Energy Environ. Sci.*, 2014, **7**, 416−426.
42 S. Choudhury, S. Stalin, D. Vu, A. Warren, Y. Deng, P. Biswal and L. Archer, *Nat. Commun.*, 2019, **10**, 4398.
43 H. Vogel, *Phys. Z.*, 1921, **22**, 645−646.
44 S. G. Fulcher, *J. Am. Ceram. Soc.*, 1925, **8**, 339−355.

45 G. Tamman and W. Hesse, *Z. Anorg. Allg. Chem.*, 1926, **156**, 245−257.
46 B. L. Papke, M. A. Rotner and D. F. Shriver, *J. Electrochem. Soc.*, 1982, **129**, 1434−1438.
47 J. E. Katon and W. R. Feairheller, *Spectrochim. Acta*, 1965, **21**, 199−201.
48 I. Ray, P. Johansson, J. Lindgren, J. C. Lassè, J. Crondin and L. Servant, *J. Phys. Chem. A*, 1998, **102**, 3249-3258.
49 H. Watanabe, N. Arai, E. Nozaki, J. Han, K. Fujii, K. Ikeda, T. Otomo, K. Ueno, K. Dokko, M. Watanabe, Y. Kameda and Y. Umebayashi, *J. Phys. Chem. B*, 2021, **125**, 7477−7484.
50 K. Fujii, H. Wakamatsu, Y. Todorov, N. Yoshimoto and M. Morita, *J. Phys. Chem. B*, 2016, **120**, 17196−17204.
51 Y. Yamada, K. Furukawa, K. Sodeyama, K. Kikuchi, M. Yaegashi, Y. Takeyama and A. Yamada, *J. Am. Chem. Soc.*, 2014, **136**, 5039−5046.
52 Y. Umebayashi, K. Matsumoto, M. Watanabe, K. Katoh and S. Ishiguro, *Anal. Sci.*, 2001, **17**, 323−326.
53 R. Bouchet, S. Lascaud and M. Rosso, *J. Electrochem. Soc.*, 2003, **150**, A1385−A1389.
54 A. Teyssot, M. Rosso, R. Bouchet and S. Lascaud, *Solid State Ionics*, 2006, **177**, 141−143.
55 S. Seki, Y. Kobayashi, H. Miyashiro, A. Yamanaka, Y. Mita and T. Iwahori, *J. Power Sources*, 2005, **146**, 741−744.
56 M. Kato, K. Hiraoka and S. Seki, *J. Electrochem. Soc.*, 2020, **167**, 070559.
57 S. Liu, N. Imanishi, T. Zhang, A. Hirano, Y. Takeda, O. Yamamoto and J. Yang, *J. Power Sources*, 2010, **195**, 6847−6853.
58 Y. Ugata, R. Tatara, T. Mandai, K. Ueno, M. Watanabe and K. Dokko, *ACS Appl. Energy Mater.*, 2021, **4**, 1851−1859.
59 X. Ren, S. Chen, H. Lee, D. Mei, M. H. Engelhard, S. D. Burton, W. Zhao, J. Zheng, Q. Li, M. S. Ding, M. Schroeder, J. Alvarado, K. Xu, Y. S. Meng, J. Liu, J. G. Zhang and W. Xu, *Chem.*, 2018, **4**, 1877−1892.
60 Y. Yamada, K. Usui, C. H. Chiang, K. Kikuchi, K. Furukawa and A. Yamada, *ACS Appl. Mater. Interfaces*, 2014, **6**, 10892−10899.
61 Y. Maeyoshi, D. Ding, M. Kubota, H. Ueda, K. Abe, K. Kanamura and H. Abe, *ACS Appl. Mater. Interfaces*, 2019, **11**, 25833−25843.
62 T. Doi, H. Oae and M. Inaba, *Electrochem. Sci. Adv.*, 2021, e2100058.
63 F. Sagane, T. Abe and Z. Ogumi, *J. Phys. Chem. C*, 2009, **113**, 20135−20138.
64 K. Yoshida, M. Tsuchiya, N. Tachikawa, K. Dokko and M. Watanabe, *J. Phys. Chem. C*, 2011, **115**, 18384−18394.
65 Y. Kobayashi, Y. Mita, S. Seki, Y. Ohno, H. Miyashiro and N. Terada, *J. Electrochem. Soc.*, 2007, **154**, A677−A681.
66 M. J. Ross, *J. Chem. Phys.*, 1974, **61**, 3977−3996.
67 S. Seki, Y. Ohno, H. Miyashiro, Y. Kobayashi, A. Usami, Y. Mita, N. Terada, K. Hayamizu, S. Tsuzuki and M. Watanabe, *J. Electrochem. Soc.*, 2008, **155**, A421−427.
68 Q. Zheng, D. M. Pesko, B. M. Savoie, K. Timachova, A. L. Hasan, M. C. Smith, T. F. Miller, G. W. Coates and N. P. Balasara, *Macromolecules*, 2018, **51**, 2847−2858.